

# Precise and High-Load Capacity Miniature 6-DOF Manipulator for Microsurgery

Liang Li , Heng Li, Chaoye Sui, Hui Ding , Bin Liu , Jianqing Li, and Guangzhi Wang 

**Abstract**—Miniaturized manipulators are invaluable for microsurgery; however, they often face limitations in precision, load capacity, and Degrees of Freedom (DOFs) due to size and weight constraints. In this article, we introduce a 6-DOF mini manipulator designed to address these challenges. Powered by cost-effective stepper linear motion modules, the proposed device incorporates a dual-plane mechanism for 4-DOF XY motion. We also innovatively integrated a compliant 2-DOF rod drive system for Z-axis rotation and translation. The manipulator's forward/inverse and remote center of motion kinematics models are provided. Furthermore, we developed a microsurgical platform equipped with microvision sensing and remote-control functions. This manipulator, which weighs less than 72 g, enables precise 6-DOF control for tools with diameters less than 0.5 mm. It delivers more than 3 N of thrust force along the compliant rod drive axis, achieving at least 10  $\mu\text{m}$  motion resolution and a 9 N maximum output force per DOF. Rigorous testing was performed, demonstrating

the system's ability to successfully perform puncture and drilling operations on porcine skin and bone. Additionally, we showed its effectiveness in ocular surgeries, demonstrating its potential for use as a cost-effective, portable device in minimally invasive procedures.

**Index Terms**—Compliant rod, dual-plane mechanism, lightweight surgical robots, mini manipulator, ocular surgeries.

## I. INTRODUCTION

ACHIEVING precise surgical interventions in living organisms has long been a pursuit of researchers in the field of robotics [1]. Numerous surgical robots have been developed [2], [3] for procedures involving both soft [4] and hard tissues [5], [6]. However, current robot-assisted surgeries primarily target larger lesion areas, and performing surgical procedures on smaller, anatomically complex regions remains a challenge for robotic systems.

The manipulation of small-scale tissues is prevalent in both clinical and scientific fields. In clinical practice, vessels with diameters of 300–800  $\mu\text{m}$  need to be connected during lymphatic flow and vascularized tissue transplantation [7]. Retinal vein cannulation surgery also addresses branch retinal veins that are less than 200  $\mu\text{m}$  in diameter [8]. Similarly, in life science research, precise microsurgical procedures are crucial, especially in small animal surgeries such as stereotactic injections in infant mice [9], punctures in functional brain regions [10], and blastocyst biopsies [11]. These surgeries often involve target tissues that are only a few tens of microns in size, making microsurgical interventions indispensable.

Several commercial surgical robots have been developed for microsurgery, including the Symani surgical system, Micro-Sure's Musa system [7], [12], the Preceyes system [13], [14], the Neuro sewing system [15], [16], and the Brainsight Vet Robot system for mouse and marmoset brain localization and guided surgeries [17]. Although these systems have demonstrated good performance in their respective tasks, they still have certain limitations. First, existing systems tend to be large, and larger manipulators occupy valuable surgical space. Furthermore, the larger size of these systems limits their portability and applicability in scenarios such as emergency rescue and field assistance. Moreover, commercial systems are expensive, which restricts their use in economically underdeveloped regions or in life sciences research involving small animal surgeries.

Manuscript received 16 February 2024; revised 7 May 2024; accepted 17 June 2024. Date of publication 11 July 2024; date of current version 18 June 2025. Recommended by Technical Editor J. Ren and Senior Editor J. Ueda. This work was supported in part by the National Natural Science Foundation of China under Grant U20A20389, Grant 81871444, Grant 62071241, Grant 62075098, Grant 62001240, and Grant U22A20355, in part by the Natural Science Foundation of Jiangsu Province China under Grant BK20230301, in part by the Natural Science Foundation of the Jiangsu Higher Education Institutions of China under Grant 23KJB310010, in part by the National Key Research and Development Program of China under Grant 2023YFC3603603, Grant 2022YFC2405600, and Grant 2022YFC2405304, in part by the Leading-edge Technology and Basic Research Program of Jiangsu under Grant BK20192004D, in part by the Key Research and Development Program of Jiangsu under Grant BE2022160, and in part by Guoqiang Institute, Tsinghua University. (Corresponding authors: Bin Liu; Guangzhi Wang.)

Liang Li is with the School of Biomedical Engineering and Informatics, Nanjing Medical University, Nanjing 211100, China, and also with the Engineering Research Center of Intelligent Theranostics Technology and Instruments, Ministry of Education, Nanjing 211100, China (e-mail: liliang@njmu.edu.cn).

Heng Li, Chaoye Sui, Hui Ding, and Guangzhi Wang are with the Department of Biomedical Engineering, School of Medicine, Tsinghua University, Beijing 100084, China (e-mail: liheng18@mails.tsinghua.edu.cn; scy21@mails.tsinghua.edu.cn; dinghui@tsinghua.edu.cn; wgz-dea@tsinghua.edu.cn).

Bin Liu is with the School of Biomedical Engineering and Informatics, Nanjing Medical University, Nanjing 211100, China, and also with the Engineering Research Center of Intelligent Theranostics Technology and Instruments, Ministry of Education, Nanjing 211100, China (e-mail: liubin@njmu.edu.cn).

Jianqing Li is with the School of Biomedical Engineering and Informatics, Nanjing Medical University, Nanjing 211100, China, and also with the Engineering Research Center of Intelligent Theranostics Technology and Instruments, Ministry of Education, Nanjing 211100, China (e-mail: jqli@njmu.edu.cn).

Color versions of one or more figures in this article are available at <https://doi.org/10.1109/TMECH.2024.3417324>.

Digital Object Identifier 10.1109/TMECH.2024.3417324



TABLE I  
COMPARISON OF MINIATURIZED MANIPULATOR

Description	Feature	Mass	Accuracy	Payload	Size (mm)
Suzuki and Wood [21]	3DOF, RCM enable	2.4 g	26.4 $\mu\text{m}$	27 mN	57 $\times$ 70 $\times$ 50
Zhang et al. [22]	3DOF, RCM enable	280 g	/	>10 mN	42 $\times$ 44 $\times$ 205
Sakai et al. [23]	5-DOF, RCM enable	770 g	40.0 $\mu\text{m}$	489 mN	85 $\times$ 100 $\times$ 240
Li et al. [24]	4-DOF, RCM unable	73 g	1.2 mm	/	50 $\times$ 50 $\times$ 40
This article	6-DOF, RCM enable	72 g	10 $\mu\text{m}$	3 N for Z and 1 N for X/Y	75 $\times$ 53 $\times$ 71

Miniature manipulators offer significant advantages in terms of space utilization, portability, and precision. Therefore, miniature manipulators have been a focal point in robotics research [18], [19], [20]. Suzuki and Wood [21] introduced an origami-inspired micromanipulator weighing only 2.4 g. This system had 3 DOFs in the remote center of motion (RCM), with a positioning accuracy of 26.4  $\mu\text{m}$  and an output force of 27 mN. Zhang et al. [22] proposed a compact 3-DOF continuum manipulator weighing 280 g, which enabled continuous spatial bending up to  $\pm 45^\circ$ . Sakai et al. [23] reported a miniaturized parallel robotic mechanism for ophthalmic surgery, weighing 770 g. This system achieved a tracking accuracy of 40  $\mu\text{m}$ . Li et al. [24] proposed a cable-driven neuro interventional robot with an external drive mechanism. The robotic motion mechanism weighed 73 g and measured 50 mm  $\times$  50 mm  $\times$  40 mm, achieving a tracking accuracy of approximately 1.2 mm. Despite numerous reported works, addressing the performance tradeoffs resulting from size and weight reduction remains a critical challenge for miniaturized surgical robots. For instance, origami-inspired manipulators produce an output force of only 27 mN [21], while continuum micromanipulators demonstrate nonlinear phenomena in terms of bending accuracy [22]. Furthermore, important challenges in balancing DOFs, weight, scale, structural complexity, and motion control complexity must be addressed for other systems [22], [23], [25].

In Table I, we summarize the miniature manipulators currently used for microsurgery. Compared with other works, this article presents a lightweight, low-cost manipulator with 6 DOFs that produces sufficient output force and precision. The primary works of this article are as follows.

- 1) We propose a modular miniature 6-DOF manipulator capable of generating up to 3 N of force with 10  $\mu\text{m}$  motion resolution. Based on the manipulator, a robotic surgical platform was developed that enables microsurgical procedures such as drilling, puncturing, and drug injection.
- 2) Based on the dual-planar parallel mechanism, we introduced a novel compliant rod-based feed and rotational degree of freedom integration approach, achieving a compact, and lightweight 6-DOF manipulator mechanism design.
- 3) We establish a kinematic model and an RCM model for the manipulator, along with a compensation model for the compliant rod, enabling effective control of the manipulator and providing a basis for quantitative analysis of the kinematics and mechanical characteristics of the manipulator integrated with the compliant rod.

## II. METHOD

### A. System Overview

The designed manipulator is shown in Fig. 1(a). First, a dual-plane parallel mechanism was used to adjust the 4-DOF motion of the surgical tool pose. Subsequently, we considered two additional DOFs for tool feeding and rotation. Considering the precision, size, and cost of the device, we adopted a miniature stepper motor-reducer-lead screw structure to realize basic robot motion. We also devised a modular system integration scheme to ensure the stability and reliability of the manipulator.

### B. Mechanical Structure Design

1) *Dual-Plane Parallel Guiding Mechanism*: Guiding mechanisms are used to facilitate the positioning and orientation of surgical tools. A dual-plane parallel mechanism was designed to fulfill the guiding function. As shown in Fig. 1(b), two linear actuators are arranged on parallel planes at a distance of  $h$ . The end points of the actuators can move freely within the planes. The spherical motion pairs are used to connect the end points of the upper and lower planes, enabling rigid body movement with 4 DOFs. Here, we connect the robotic guiding sleeve with two spherical motion pairs to the driving mechanism. The linear actuators of the upper and lower planes are arranged in parallel, allowing manipulation of the position and orientation of the guiding mechanism by controlling the actuators.

2) *Compliant Rod-Driven Feeding Mechanism*: The feeding mechanism is primarily responsible for the insertion and rotational DOFs of the end effector. As shown in Fig. 1(b), the tool is controlled by a linear motion motor, while the rotational motion is controlled by a rotary motor. Considering that different surgical tasks may have varying requirements, we propose a replaceable end effector rotation motor scheme using a slot structure. This enables the robot to select different types of rotation motors according to the specific task requirements.

Considering the limited load-bearing capacity of the miniature manipulator system, we employed a compliant rod transmission method. As shown in Fig. 1(a) and (b), a superelastic compliant rod (made of nickel-titanium alloy) was applied to connect the surgical instrument and the rotary motor. The compliant rod transmits thrust and torque, while the guiding mechanism adjusts the position and orientation of the instrument by manipulating the instrument guide rod. This approach decouples the guiding and feeding mechanisms at the mechanical level, allowing independent control of the guiding and feeding processes. This approach greatly simplifies the structure of the manipulator.



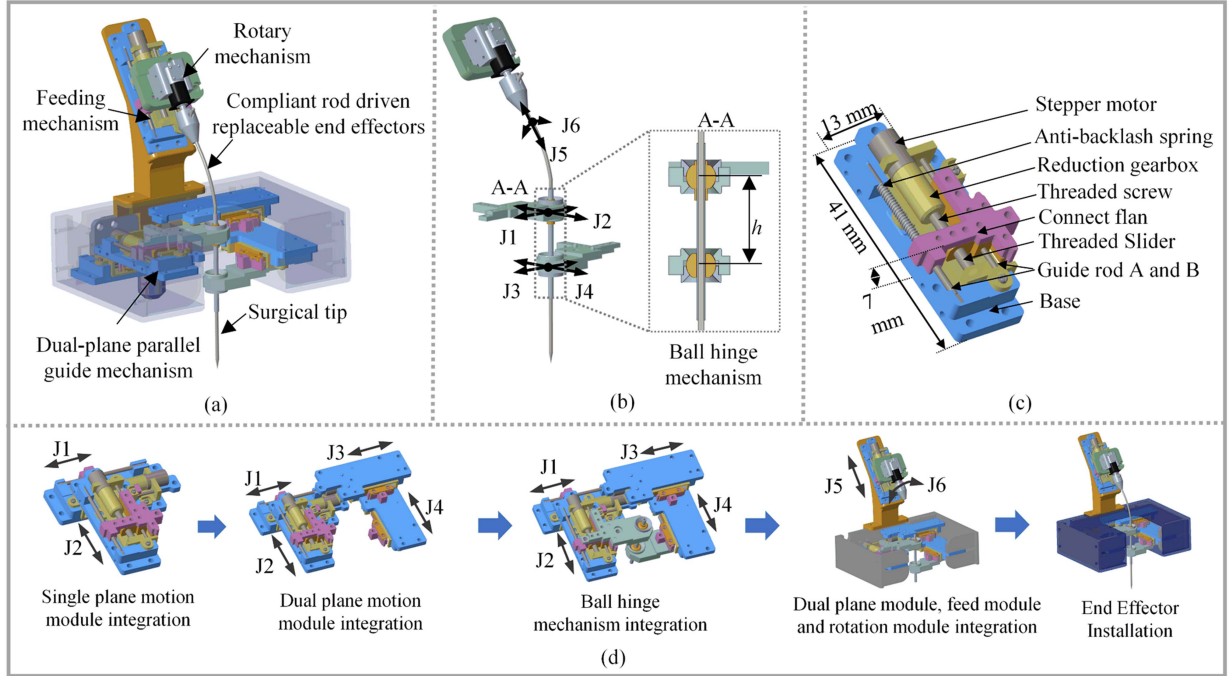


Fig. 1. Overall structure design and assembly method of the manipulator. (a) Structure of the manipulator. (b) Distribution of the DOFs and the principles of motion for each DOF. (c) Motion unit of the manipulator. (d) Construction process of the manipulator.

**3) Drive Units:** To meet the requirements of miniaturization, weight, precision, load capacity, and cost for the micro manipulator, a mini linear actuator was adopted as the actuation unit. As shown in Fig. 1(c), this actuator weighs only 2.7 g and has a stroke of 8 mm. It consists of a miniature stepper motor, a planetary gearbox, and a lead screw. Due to the inherent characteristics of the stepper motor, the actuator motion distance can be directly obtained through open-loop control commands. Moreover, due to the combination of the gearbox and lead screw transmission, the miniature stepper motor has sufficient output force and motion resolution. Considering that clearance is a critical factor leading to transmission errors in motor-gear-screw arrangements, we optimized the transmission clearance of this linear unit. As depicted in Fig. 1(c), a spring preload method is employed to control the clearance direction in the mechanical transmission process, thereby ensuring a defined clearance size for the drive unit.

**4) Assembly and Manufacturing:** We adopt a modular approach to the manufacturing of the manipulator, enabling mass production and improving the system's interchangeability and expandability. The manufacturing process of the robotic manipulator is depicted in Fig. 1(d). We designed standardized drive units and connection interfaces. The guiding mechanism is composed of four identical drive units. The feeding mechanism in the feeding DOF is composed of standardized drive units, while the drive units for the rotational DOFs are individually customized based on specific surgical requirements.

### C. Kinematics Model of the Manipulator

**1) Definition of the Coordinate Systems:** As shown in Fig. 2, we define  $O_{tool}$  as the tip of the surgical tool and  $O_0$ ,  $O_1$  as the

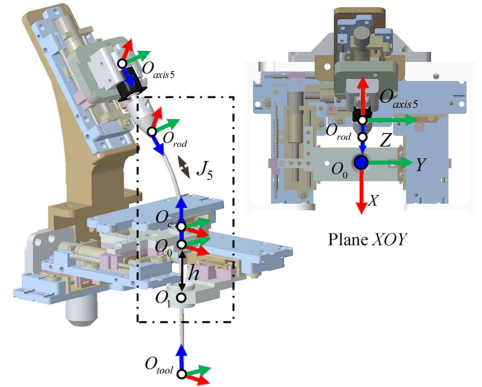


Fig. 2. Definition of the coordinate systems.

center points of the ball joint in the upper and lower planes, respectively.  $O_c$  is the connection point between the compliant rod and the guide sleeve,  $O_{rod}$  is the fixed end point of the compliant rod, and  $O_{axis5}$  is the point on the base of the manipulator's fifth axis. For convenience in the calculations, we established a coordinate system at each of the above points, with the origin of the coordinate system coinciding with the corresponding point and the direction of the coordinate system set as shown in Fig. 2.

**2) Kinematic Model of the Dual-planar Mechanism:** The dual-planar parallel mechanism is a classic structure for adjusting the pose of surgical tools [26], [27], [28]. Fig. 3 depicts the kinematic relationships of the mechanism in the  $YOZ$  and the  $XOZ$  planes within the manipulator's base coordinate system.

The coordinates of points  $O_0$  and  $O_1$  in the manipulator base coordinate system are  $(x_{O_0}, y_{O_0}, 0)$  and  $(x_{O_1}, y_{O_1}, h)$ , respectively, where  $x_{O_0}$ ,  $y_{O_0}$ ,  $x_{O_1}$ , and  $y_{O_1}$  are controlled by



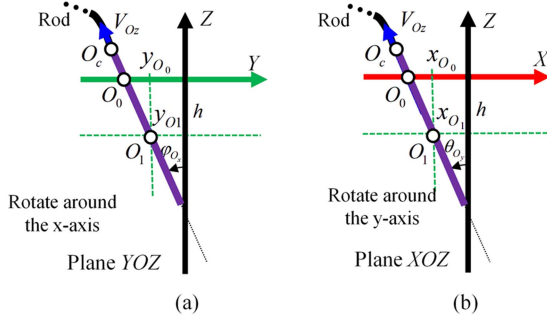


Fig. 3. Kinematic model of the dual-planar mechanism in the YOZ and XOZ planes.

driving units 1–4 and  $h$  represents the distance between the two planes. The rotation angle of the robot's flange coordinate system around the  $X$ -axis is  $\varphi_{O_x} = -\tan((y_{O_0} - y_{O_1})/h)^{-1}$ , and that around the  $Y$ -axis is  $\theta_{O_y} = \tan((x_{O_0} - x_{O_1})/h)^{-1}$ . Thus, we can obtain the translation and rotation matrix (1) in the  $XY$ -direction of the surgical tool relative to the base coordinate system. In this article, the functions **Rot**() and **Trans**() are calculated from the (s1) and (s2) in the Appendix

$${}^{\text{base}}\mathbf{T}_{\text{flan}} = \begin{bmatrix} \mathbf{Rot}(0, \theta_{O_y}, \varphi_{O_x}) & \mathbf{0} \\ \mathbf{0} & 1 \end{bmatrix} \cdot \mathbf{Trans}(x_{O_0}, y_{O_0}, 0). \quad (1)$$

**3) Kinematic Model of the Compliant Rod:** In this section, we derive the kinematic model for the extension and rotation motion of the manipulator's tip. Let  $l_{O_0\text{--}tool}$  denote the distance between points  $O_0$  and  $O_{tool}$ .  $l_{O_1\text{--}tool}$  can be calculated using (2), considering the compliant rod bending and angle changes in the  $XY$ -direction during manipulator motion

$$l_{O_0\text{--}tool} = l_{\text{axis5}} + L_{O_1\text{--}tool} + l_{O_0O_1} + \Delta l_{\text{rod}} \quad (2)$$

where  $l_{\text{axis5}}$  represents the extension of the fifth-axis motion unit,  $L_{O_1\text{--}tool}$  represents the distance from point  $O_1$  to the origin of the tool coordinate system in the initial position (which is a fixed value determined during tool manufacturing), and  $l_{O_0O_1}$  represents the distance between points  $O_0$  and  $O_1$ . According to the triangle relationship,  $l_{O_0O_1}$  can be calculated as  $l_{O_0O_1} = h / \arctan(\tan \theta_{O_y} \cdot \tan \varphi_{O_x})$ . When the end effector rotates around the  $X$ - and  $Y$ -axes, this distance changes.  $\Delta l_{\text{rod}}$  represents the length change caused by the bending of the compliant rod. To determine the distribution of the rod length with respect to changes in the position and orientation of the manipulator's end effector, we modeled the compliant rod.

As shown in Fig. 4, the compliant rod in the manipulator can be regarded as a cantilever beam with one end fixed to the fifth motion unit. A sleeve is used to constrain the free end of the cantilever beam at point  $O_c$ , allowing it to bend under certain translation and rotation conditions (the free end can slide within the sleeve). The changes in the position and orientation of the free end of the cantilever beam relative to the fixed end can be obtained using the spatial coordinate relationship shown in

$${}^{\text{rod}}\mathbf{T}_{O_c} = {}^{\text{rod}}\mathbf{T}_{\text{axis5}} {}^{\text{axis5}}\mathbf{T}_{\text{base}} {}^{\text{base}}\mathbf{T}_{\text{flan}} {}^{\text{flan}}\mathbf{T}_{O_c} \quad (3)$$

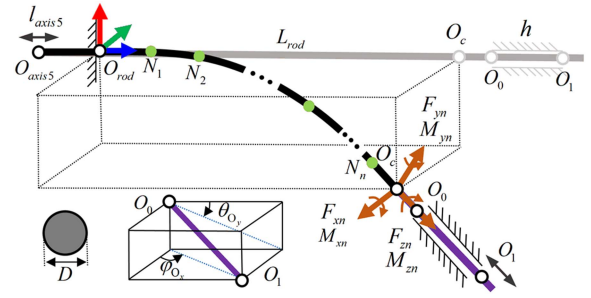


Fig. 4. Chained spatial-beam constraint model of the compliant rod.

where  ${}^{\text{rod}}\mathbf{T}_{\text{axis5}} = \mathbf{Trans}(0, 0, l_{\text{axis5}})$  represents the transformation matrix for the base of the manipulator's fifth axis to the fixed point of the compliant rod. This matrix is a function of the length  $l_{\text{axis5}}$  of the fifth-axis motion unit.  ${}^{\text{axis5}}\mathbf{T}_{\text{base}}$  represents the transformation matrix from the fifth axis of the manipulator to its base coordinate system.  ${}^{\text{flan}}\mathbf{T}_{O_c}$  represents the transformation matrix from the constraint point of the compliant rod's free end to the flange coordinate system. These three matrices can be obtained using the Denavit–Hartenberg method [29] based on the geometric dimensions of the manipulator. The fourth matrix  ${}^{\text{base}}\mathbf{T}_{\text{flan}}$  is a function of  $x_{O_0}$ ,  $y_{O_0}$ ,  $x_{O_1}$ , and  $y_{O_1}$ , obtained from (1).

According to (3), we can obtain the pose of the compliant rod's free end relative to the fixed end at any position on the manipulator's first to fifth axes. We introduce the chained spatial-beam constraint model (CSBCM) to model the compliant rod [30]. As shown in Fig. 4, the compliant rod can be equivalently divided into  $n$  segments of small compliant rods (from  $N_1, N_2$  to  $N_n$ ), with the bending of each small segment modeled using the chained beam constraint model [31]. All the small segments are connected through spatial coordinate transformations, forming a chain-like deformation structure. The diameter of the rod is  $D$  and the length of the rod before bending is  $L_{\text{rod}}$ . Since the position and orientation of the compliant rod's free end are known, we can establish the system of equations represented as

$${}^{\text{rod}}\mathbf{T}_{O_c} = f_{\text{CSBCM}}(\mathbf{F}_n, \mathbf{M}_n, l_{\text{rod}}). \quad (4)$$

Here,  $\mathbf{F}_n = [F_{xn}, F_{yn}, F_{zn}]$ ,  $\mathbf{M}_n = [M_{xn}, M_{yn}, M_{zn}]$  represent the applied forces and torques on the compliant rod's free end, respectively.  $l_{\text{rod}}$  represents the actual length of the compliant rod under this constraint. By solving the equations in (4), we can obtain the length of the compliant rod at any position of the manipulator. We use the Levenberg–Marquardt method [32] to solve (4). Taking the rod length  $l_{\text{rod\_ref}}$  of the initial position of the manipulator as a reference, we have  $\Delta l_{\text{rod}} = l_{\text{rod}} - l_{\text{rod\_ref}}$ . Thus, according to (2), the  $Z$ -axis displacement of the manipulator's tip can be calculated.

The torque at the fixed end of the compliant rod can be approximately transmitted without loss to the tip of the compliant rod. Therefore, the  $Z$ -axis rotation angle of the manipulator can be obtained as  $\psi_{O_{\text{tool}}} = \psi_{O_0} = \psi_{O_c} = \psi_{O_{\text{rod}}} = \psi$ , where the angle  $\psi$  is controlled by the sixth drive unit of the manipulator. The



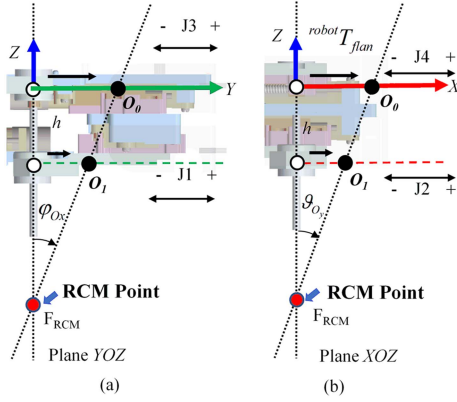


Fig. 5. RCM models of the manipulator in the YOZ and XOZ planes.

transformation matrix from the tool coordinate system to the flange coordinate system can be expressed as shown in (5). Ultimately, the coordinate transformation relationship from the tool endpoint to the manipulator's base coordinate system can be represented by  ${}^{\text{base}}\mathbf{T}_{\text{tool}} = {}^{\text{base}}\mathbf{T}_{\text{flan}} \cdot {}^{\text{flan}}\mathbf{T}_{\text{tool}}$

$${}^{\text{flan}}\mathbf{T}_{\text{tool}} = \begin{bmatrix} \text{Rot}(\psi, 0, 0) & \mathbf{0} \\ \mathbf{0} & 1 \end{bmatrix} \cdot \text{Trans}(0, 0, l_{O_0\text{-tool}}). \quad (5)$$

4) *Inverse Kinematics of the Manipulator*: The inverse kinematics can also be calculated in two steps. First, the motion values for the first to fifth drive units are calculated based on the pose vector  $V'_{\text{flan}} = [x_{\text{flan}}, y_{\text{flan}}, 0, \varphi_{\text{flan}}, \vartheta_{\text{flan}}, 0]$  in the flange coordinate system. This part can be solved by conventional methods [26], [27], [28].

Then, the flange-to-tool coordinate matrix  ${}^{\text{flan}}\mathbf{T}_{\text{tool}}$  is solved according to the coordinate matrix  ${}^{\text{base}}\mathbf{T}_{\text{tool}}$  of the surgical tool and the matrix  ${}^{\text{base}}\mathbf{T}_{\text{flan}}$  of the flange coordinate system, where  ${}^{\text{flan}}\mathbf{T}_{\text{tool}} = ({}^{\text{base}}\mathbf{T}_{\text{flan}})^{-1} \cdot {}^{\text{base}}\mathbf{T}_{\text{tool}}$ . According to (5), the matrix  ${}^{\text{flan}}\mathbf{T}_{\text{tool}}$  includes only the translation along the Z-axis  $l_{O_0\text{-tool}}$  and the rotation angle  $\psi$  around the Z-axis. Since the position and orientation of the manipulator's flange are already known, according to (2), the control input for the fifth axis motion unit is  $l_{\text{axis5}} = l_{O_0\text{-tool}} - (L_{O_0\text{-tool}} + l_{O_1O_2} + \Delta l_{\text{rod}})$ . For the rotation angle around the Z-axis, based on the design of the compliant rod, only the angular displacement of the 6th axis motion unit must be controlled to match the target angle  $\psi$ .

#### D. RCM Kinematics

The RCM of the designed manipulator can be determined, and the RCM point can be adjusted. As shown in Fig. 5, for the designed manipulator, all guiding motions are achieved by changing the positions of the motor-driven points  $O_0$  and  $O_1$ . Therefore, to determine the RCM, it is necessary to ensure that the manipulation points  $O_0$  and  $O_1$  the RCM point always lie in a straight line. That is,  $\overrightarrow{O_1F_{\text{RCM}}} = n\overrightarrow{O_0F_{\text{RCM}}}$ . The proportion coefficient  $n$  can be calculated based on the trigonometric relationships, represented as

$$n = \frac{z_{O_0} - z_{F_{\text{RCM}}}}{(z_{O_0} - z_{F_{\text{RCM}}}) - h} = \frac{y_{O_0} - y_{F_{\text{RCM}}}}{y_{O_1} - y_{F_{\text{RCM}}}} = \frac{x_{O_0} - x_{F_{\text{RCM}}}}{x_{O_1} - x_{F_{\text{RCM}}}}. \quad (6)$$

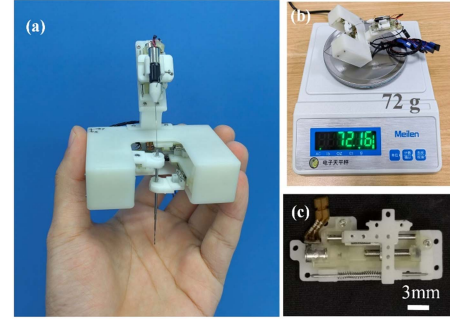


Fig. 6. Prototype of the lightweight 6-DOF manipulator. (a) Constructed manipulator. (b) Overall mass of the manipulator. (c) The driver unit.

Let  $\varphi_{ox}$  denote the rotational angle of the tool around the X-axis direction of the RCM point and  $\theta_{oy}$  represent the rotational angle of the tool around the Y-axis direction of the RCM point. The constraint expressions for RCM rotation can be obtained as

$$\tan(-\varphi_{ox}) = \frac{y_{O_{\text{up}}} - y_{F_{\text{RCM}}}}{z_{O_{\text{up}}} - z_{F_{\text{RCM}}}} \quad (7)$$

$$\tan(\theta_{oy}) = \frac{x_{O_{\text{up}}} - x_{F_{\text{RCM}}}}{z_{O_{\text{up}}} - z_{F_{\text{RCM}}}}. \quad (8)$$

From the above equations, the mathematical relationships between the control points in the upper and lower planes can be derived when the manipulator performs RCM, as shown in (9)–(12). Here,  $x_{F_{\text{RCM}}}$  and  $y_{F_{\text{RCM}}}$  represent the coordinates of the RCM point

$$y_{O_0} = \tan(-\varphi_{ox}) \cdot (z_{O_0} - z_{F_{\text{RCM}}}) + y_{F_{\text{RCM}}} \quad (9)$$

$$x_{O_0} = \tan(\theta_{oy}) \cdot (z_{O_0} - z_{F_{\text{RCM}}}) + x_{F_{\text{RCM}}} \quad (10)$$

$$y_{O_1} = (y_{O_0} - y_{F_{\text{RCM}}})/n + y_{F_{\text{RCM}}} \quad (11)$$

$$x_{O_1} = (x_{O_0} - x_{F_{\text{RCM}}})/n + x_{F_{\text{RCM}}}. \quad (12)$$

Equations (9)–(12) provide the geometric constraint relationships between the lower and upper manipulation points when the manipulator performs RCM. As long as the positions of points  $O_0$  and  $O_1$  satisfy the positional relationships described by (9)–(12), the manipulator can execute the RCM, and the RCM point can be set according to specific requirements.

### III. RESULTS

The results are presented from four aspects. First, the prototype system was constructed. Then, the performance of the system was tested, followed by functional testing. Finally, a preliminary application of the system was evaluated.

#### A. Prototype System Construction

1) *Prototype System*: Fig. 6(a), (b), and (c) shows the prototype of the manipulator and a driver unit. The mass of a single manipulator is 72 g (Including a cover mass of 15 g, and six cables weighing 6 g), and the dimensions of 75 mm × 53 mm × 71 mm.



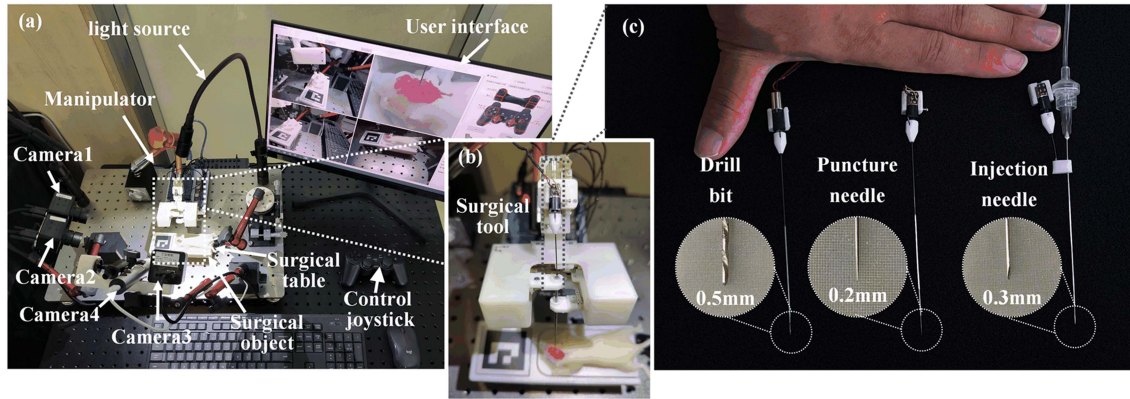


Fig. 7. System for testing the manipulator. (a) Testing workstation, including the manipulator, observation cameras, GUI interface and control joystick. (b) Manipulator, surgical tools, and simulated surgical target. (c) Three type surgical tools used for the manipulator.

**2) Integration of the Manipulator:** We developed a microsurgical operating platform to test the effectiveness of the manipulator. The system consisted of three cameras with 4 mm focal lengths (XW800, Micro Precision, China) and one telephoto microscope camera (B013 camera, L400 lens, 30–400x magnification field of view, Shenzhen Super Vision Company, Ltd., China). Two of the cameras were set at fixed positions to form a stereo vision camera, which is used for spatial localization in stereoscopic vision. The telephoto microscope camera and another 4 mm camera provided alternative views of the surgical tools and the surgical target. Additionally, a remote-controlled handheld device was used for wireless control of the manipulator. The integrated system is shown in Fig. 7(a) and (b).

The designed manipulator could be used to control various microsurgical tools. We designed three commonly used surgical tools, as shown in Fig. 7(c). All tools were mounted on the fifth-DOF joint of the manipulator using standardized structures and had rotational freedom via separate motors.

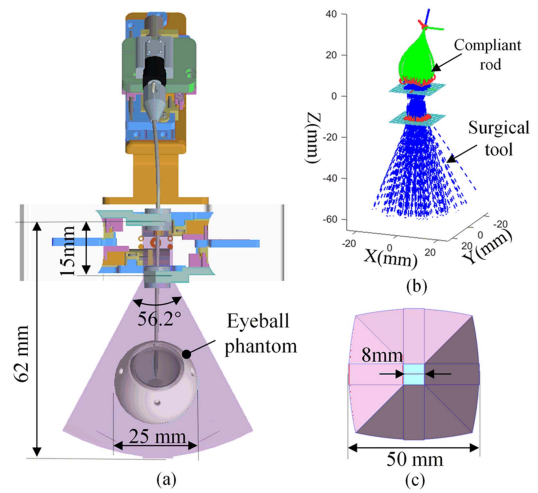


Fig. 8. Workspace of the proposed manipulator. (a) Front views of the workspace. (b) Simulation results of the workspace using the Monte Carlo method. (c) Top views of the workspace.

## B. Performance Testing

**1) Workspace Analysis:** The workspace of the manipulator is shown in Fig. 8(a), and (c) shows the front and top views of the workspace. We superimposed the manipulator and a 25 mm diameter eyeball phantom in the front view of the workspace to intuitively demonstrate the operator's workspace coverage. Fig. 8(b) shows the simulation results of the workspace using the Monte Carlo method, demonstrating the morphological distributions of the compliant rod and surgical tools at different positions.

**2) Accuracy of the Single Drive Units:** A randomly selected drive unit was utilized to drive the optical grating scale. Motion information was obtained by reading the grating scale (China, Ditron Company, DC11, resolution of  $0.1 \mu\text{m}$ ). The test results are presented in Fig. 9(a) and (b), demonstrating that the drive units achieved 5-step and 50-step movements. The calculation results show that the drive units can achieve a motion accuracy of  $1 \pm 1 \mu\text{m}$  when moving in increments of 5 steps. When moving in increments of 50 steps, the drive units can achieve

a motion accuracy of  $10 \pm 2 \mu\text{m}$ . It can be observed that the motion resolution of a single drive unit is better than  $10 \mu\text{m}$ .

**3) Accuracy of the Dual-planar Mechanism:** First, we constructed a stereovision system capable of measuring small movements based on our previous work [33]. We fixed visual markers on the guide sleeve of the parallel mechanism and used a stereo camera to record the motion trajectory of the manipulator to evaluate its rotational and translational accuracies, as shown in Fig. 9(c).

To evaluate the rotational accuracy, we first controlled the manipulator to deviate to a fixed angle. Then, using the stereo camera, we observed the angle variation of the end tool of the manipulator during translational motion in the  $XOZ$  and  $YOZ$  planes. The statistical results are shown in Fig. 9(d), where the  $X$ -axis represents the step difference between motion units  $O_0$  and  $O_1$  in the corresponding direction and the vertical axis represents the corresponding angle and its standard deviation during the translational process. In both the  $YOZ$  and  $XOZ$  planes, the constructed parallel mechanism provides a stable deviation



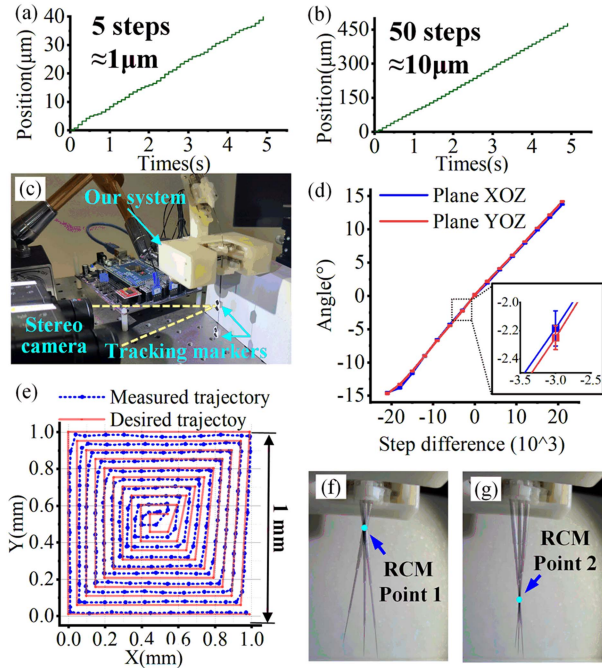


Fig. 9. Accuracy and motion capability test of the manipulator. (a) and (b) Measurement of the grating position during 5-step and 50-step motion of the drive unit. (c) Experiment to evaluate the overall motion accuracy of the manipulator system. (d) Measurement of angular accuracy. (e) Motion trajectory in the overall accuracy test of the manipulator system, compared to a standard trajectory. (f) and (g) RCM range at different RCM points.

angle. According to the statistics, the average angle variation recorded in the  $XOZ$  and  $YOZ$  directions during translational motion is  $\pm 0.09^\circ$ .

To assess the translational accuracy, we controlled the parallel mechanism to perform a rectangular trajectory while carrying visual markers. A stereo camera was used to record the motion trajectory and verify the accuracy of the system. Fig. 9(e) displays one of the measured trajectories, revealing that the designed manipulator successfully executed 10 layers of rectangular trajectory movements within a 1 mm square space (with a spacing of  $50 \mu\text{m}$ ).

In addition, we validated the RCM performance of the proposed system. Fig. 9(f) and (g) depicts the adjustable RCM capability of the manipulator. The results demonstrate that the manipulator can execute RCM at various RCM points.

**4) Accuracy of the Compliant Rod Model:** We first tested the ability of the CSBCM method to model the compliant rod of the manipulator. For testing, we set the rod diameter to 0.5 mm, Young's modulus to 65 GPa, and shear modulus to 25 GPa, and divided it into  $N = 30$  segments for computation. Fig. 10 presents a comparison between the predicted compliant rod shape from the mathematical model and the captured compliant rod shape from the camera at various positions and orientations of the surgical tool. The calculated compliant rod shape from the model aligns well with the actual compliant rod shape.

Then, we compensated for the Z-axis deviation of the surgical tool caused by the bending of the compliant rod using the fifth axis of the manipulator. Fig. 11 illustrates the results before and

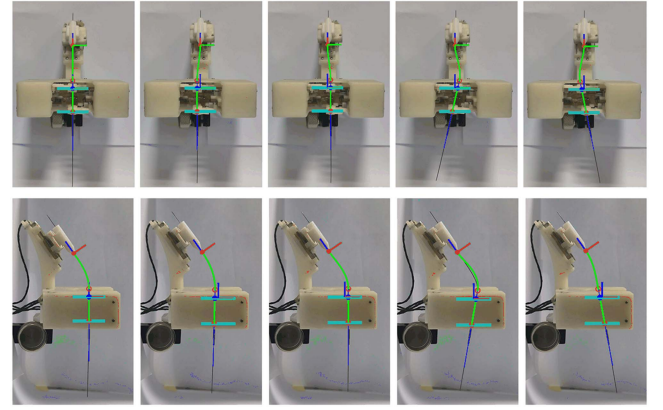


Fig. 10. Overlay of the compliant rod shape calculated by the mathematical model and the real compliant rod shape.

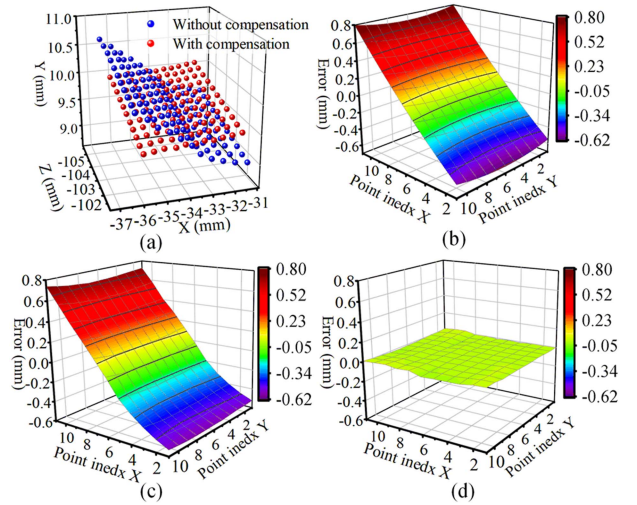


Fig. 11. Validation of Z-axis compensation accuracy. (a) Point distribution of marker point positions on the surgical tool during translational motion of the manipulator before and after compensation. (b) Z-axis deviation at different positions in the array puncture task calculated by the CSBCM model. (c) Measured Z-axis deviation without compensation. (d) Measured Z-axis deviation after compensation.

after compensation when performing an array puncture task with a  $4 \text{ mm} \times 4 \text{ mm}$  grid and a  $0.4 \text{ mm}$  spacing. In Fig. 11(a), the distribution of the tool end points before and after compensation, as measured by the stereovision camera, is shown. Fig. 11(b) represents the Z-axis deviation at different positions in the array puncture task calculated by the CSBCM model. Fig. 11(c) shows the actual measured Z-axis deviation without compensation, while Fig. 11(d) shows the Z-axis deviation after compensation.

It can be observed that, in this task, the Z-axis deviation of the tool caused by the bending of the compliant rod ranges from  $-0.56 \text{ mm}$  to  $0.74 \text{ mm}$ . However, our constructed model of the compliant rod motion can control the Z-axis deviation caused by the bending of the compliant rod within an extremely small range.

**5) Load Capacity of A Single Drive Unit:** A randomly selected drive unit was fixed onto a force gauge (China, Nscing



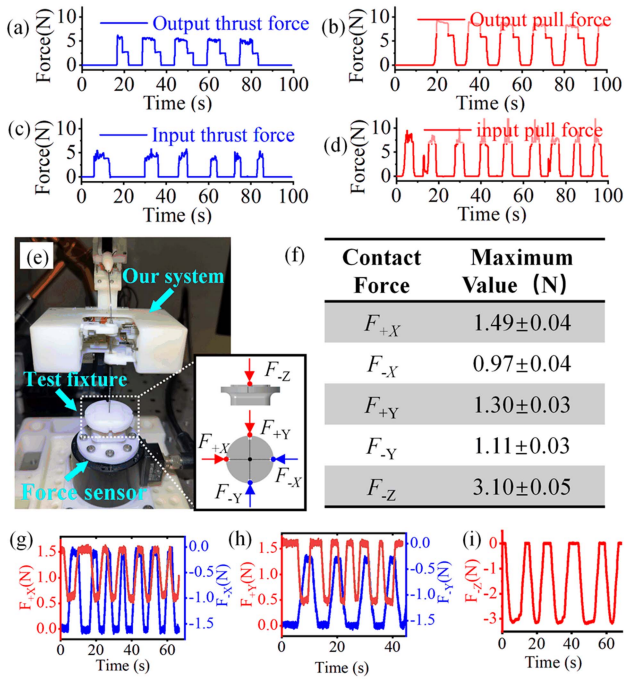


**Fig. 12.** Load Capacity of the manipulator. (a) Output thrust force of the drive unit. (b) Output tension force of the single drive unit. (c) Self-locking force of the drive unit in the pushing direction. (d) Self-locking force of the single drive unit in the pulling direction. (e) Experiment for overall load force testing of the manipulator. (f) Results of the overall load force testing in different directions at the manipulator end effector. (g) Contact force curve in the  $\pm X$ -direction at speed 2 mm/s. (h) Contact force curve in the  $\pm Y$ -direction at speed 2 mm/s. (i) Contact force curve in the  $-Z$ -direction at speed 2 mm/s.

Es/Su Measurement Company, SH-III-500, resolution of 0.1 N), and the controller was used to control the drive unit to perform pushing and pulling movements. Fig. 12(a) and (b) demonstrates that a single motion unit can provide a maximum thrust of 6 N and a maximum tension of approximately 9 N (the imbalance between the thrust and tension output is mainly due to the backlash spring). The self-locking force of the motion unit was also measured using a force gauge. Fig. 12(c) and (d) illustrates that the motion unit exhibits self-locking forces of approximately 5–6 N in the pushing direction and 7–8 N in the pulling direction. These test results indicate that the motion unit can deliver a considerable driving force while maintaining its own position even with substantial external disturbances.

**6) Load Capacity of the Whole Manipulator:** Considering that the motion of the motion unit is ultimately transmitted to the surgical tool through the compliant rod, some of the driving force may be lost. Thus, we tested the overall load capacity of the manipulator. As depicted in Fig. 12(e), we controlled the manipulator with the attached surgical tool to contact a 6-DOF force sensor (Switzerland, Bota Systems AG, MEDUSA; resolution of 0.01 N) from different directions at a constant speed. Fig. 12(f) shows the maximum output force ranges for the  $\pm X$ -,  $\pm Y$ -, and  $-Z$ -axis feeding directions, with the experiments for each direction repeated five times. Fig. 12(g), (h), and (i) depicts the variation in the force produced by the manipulator over

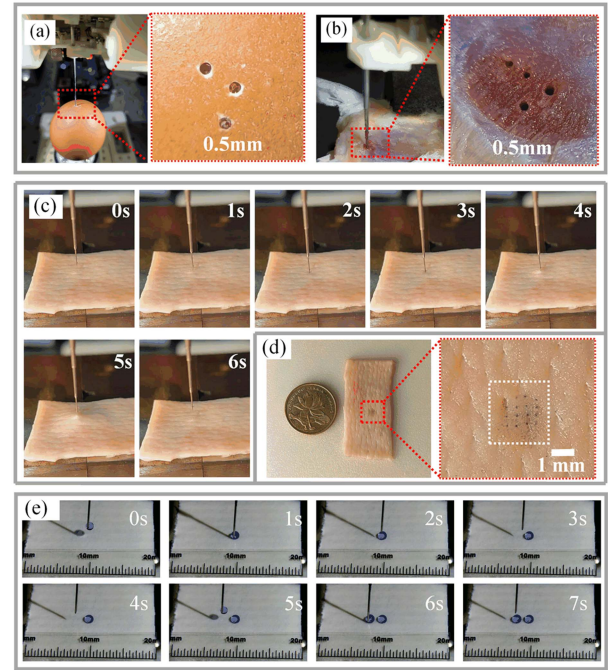


**Fig. 13.** (a) Experiment of drilling on an egg. (b) Experiment of drilling on a porcine bone. (c) Puncture experiments and the automated puncture process. (d) Microarray after puncture operation. (e) Injection and aspiration experiment, including the manipulator manipulating a droplet and an injection.

time during the testing process. The manipulator can provide an output force greater than 3 N in the  $Z$ -axis feeding direction and a driving force of approximately 1 N in the lateral motion direction ( $XY$ -plane).

### C. Function Test

To demonstrate the applicability of the system in real surgical scenarios, we conducted functional experiments using three commonly performed surgical tasks: drilling, puncturing and injection.

**1) Drilling Experiments:** We utilized the drilling tool of the constructed system to perform drilling tests on both eggs and porcine bones. A drill bit with a diameter of 0.5 mm was used, and the feed rate and rotational speed of the drill bit were remotely controlled through the joystick. As shown in Fig. 13(a) and (b), the system successfully performed the drilling tasks with both the eggshell and porcine bone tissue.

**2) Puncture Experiments:** Next, puncture experiments were conducted using the puncture needle tool. The target tissue for puncture was porcine skin. The manipulator system was programmed to puncture a  $4 \times 4$  array of 16 micro holes. Fig. 13(c) shows the automated puncture process for a single hole. Fig. 13(d) displays the final puncture array results. The results showed that the system successfully performed precise puncture tasks with porcine skin, which is both thick and tough.

**3) Injection Experiments:** Our system is also capable of performing liquid delivery and aspiration tasks. Fig. 13(e) shows the results of a simulated drug injection experiment with the



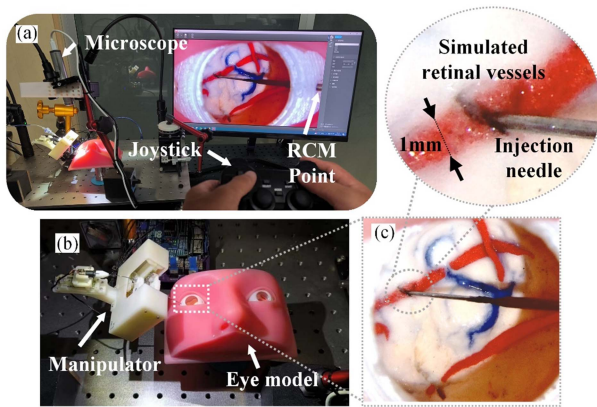


**Fig. 14.** Demonstration of the application of the manipulator in ophthalmic surgery. (a) Schematic diagram of the overall experiment. (b) Manipulator and eyeball phantom. (c) Enlarged images of the inside of the phantom eyeball.

proposed system, in which diluted blue ink was used to simulate the drug. The results show that the system can perform liquid delivery operations within confined spaces.

#### D. Application Test

The operational system we designed also holds potential for application in ocular surgery. As depicted in Fig. 14(a), we conducted retinal vessel puncture experiments using the proposed operational system. We devised an artificial eye model in which we positioned several simulated vessels with diameters less than 1 mm in the retina. The end effector of the operational tool was directed to enter the eye from the side, and utilizing RCM, the tool reached the target vessel to perform the puncture and injection procedures. During this process, the robot was controlled by the operator using a joystick. Fig. 14(b) and (c) displays the final puncture results. The results demonstrated that our designed operational system could perform puncture and injection procedures through the sides of simulated retinal vessels, each with a diameter less than 1 mm.

### IV. DISCUSSION

In this article, we introduced a 6-DOF miniaturized manipulator. We designed a dual-planar parallel mechanism to adjust the pose of surgical instruments and implemented feed and rotation mechanisms for surgical tools. We utilized compliant rods for power transmission to the guiding module to simplify the system and employed a modular manufacturing approach to enhance stability and reliability. Kinematic models for the system were also derived. Finally, we demonstrated initial applications and tests of the integrated system, verifying its performance in tasks such as bone drilling, soft tissue puncture, and drug injection.

Biological tissues exhibit a considerable degree of toughness, and when robotic surgical tools interact with these tissues, substantial contact forces are generated. Therefore, a robotic system must have adequate load-bearing capabilities. However, to maintain a compact structure, miniaturized manipulators have limitations in both their output force and self-locking capabilities

[21], [22]. The performance testing results indicate that the proposed manipulator maintains high motion resolution precision while also delivering Newton-level output forces and demonstrating self-locking capabilities. As shown in Fig. 12, at the driver unit level, each individual driver can provide thrust, tension, and self-locking forces exceeding 5 N. At the overall system level, the end of the miniaturized manipulator can provide an output force of approximately 1 N in the  $X/Y$ -direction and a thrust of more than 3 N in the  $Z$ -direction. In addition, the results of functional tests showed that the manipulator has a load capacity that matches that of biological tissue. The system can complete drilling tasks with hard biological materials (eggshell and pig bone) and puncture tasks with tough tissue (pig skin). These results demonstrate the potential of the manipulator in microsurgery.

Due to various constraints, such as spatial limitations, payload considerations, and structural complexity, researchers have reported manipulators with limited DOFs for miniaturized surgical robots [21], [22], [24]. In this article, we innovatively employed a rigid-flexible coupled method. A feasible approach involving the integration of a rigid guiding mechanism and a flexible feed-rotational mechanism is demonstrated, showing the feasibility and potential of flexible components in microsurgical operations. The results indicate that the introduction of flexible components can considerably reduce the complexity of the mechanical structure while ensuring satisfactory precision and load capacity. This article provides a reference for the design of microsurgical manipulation mechanisms.

Rigid construction results in better accuracy, but it presents a challenge regarding miniaturization. As objects become thinner, their stiffness decreases. While flexible construction approaches may lead to decreased precision, they also simplify the structural design. Moreover, they also mitigate the gaps among the mechanisms through elastic deformation. Clearly, achieving a balance between these aspects is key to effective design. In this article, we explored the application of flexible rod devices in precise microsurgical manipulation mechanisms. We demonstrate that the compliant rod system provides appropriate output forces and precise motion. Although the deformation of the compliant mechanism caused by the load is unavoidable, with the help of appropriate mathematical models or feedback measurement methods, we can compensate for these unwanted deformations while retaining the advantages of the flexible mechanism. The author believes that this idea is valuable for reference in the design of miniaturized and flexible surgical manipulators.

The utilization of the compliant rod transmission mechanism substantially simplifies the mechanical design of our 6-DOF manipulator, but several challenges should still be addressed. Specifically, as the guiding tubes of the manipulator within the dual-planar mechanism assume various positions and orientations, the relationship between the sixth-degree motor and the upper end of the guiding tube changes accordingly. Consequently, fluctuations in the length and bending of the compliant rods occur during operation, affecting the length and load-bearing capacity of the surgical tool's end effector. Although we developed the theoretical model that considers the bending of the compliant rod and the tilting of the guide pipe, solving



the compliant rod bending model requires iterative solutions to a multivariable nonlinear system of equations, which can be time-consuming and hinder real-time control by the manipulator. In future work, we will establish a data-driven model for the bending of the compliant rod to expedite the model solving process.

Another challenge concerns the force and deformation characteristics of the compliant rod. First, in terms of self-locking performance, since the output force at the system level is smaller than the self-locking force of the single drive unit (see Fig. 12), within the operating force range of the manipulator's tool, the drive unit movement can be uninterrupted by the load force. But, the tool end will produce a certain deformation displacement under operating load. Although the load force is usually small during micromanipulation, this will still affect the accuracy of the system under load. Second, due to the relatively low stiffness of the compliant rod, there may be a certain lag between the rotational motion of the tip of the flexible rod relative to the rotational motion of the motor at the tail end. To address the above issue, our manipulator currently operates in a teleoperated mode, allowing operators to make necessary adjustments and compensations for these variations.

The flexible rod model based on CSBCM established in this article provides analytical functions for the load and deformations of the rod, which serves as a valuable theoretical tool for quantitative analysis and optimization of the characteristics of the manipulator. With this model, we can determine the relationship between the self-locking force and the Z-axis displacement caused by the rod deformation. It is also possible to model the rotational lag effect caused by low stiffness of the compliant rod. Additionally, we can identify the optimal spatial relationship between the flexible rod and the guiding mechanism. Due to manuscript length constraints, we did not present the applications mentioned above. In future work, we will conduct a more in-depth analysis of the manipulator's characteristics based on this model to achieve a more optimized design of the operator's device.

## V. CONCLUSION

We propose a design scheme for a miniaturized microsurgical manipulator. The experimental results demonstrated that the manipulator is capable of performing common clinical tasks such as tissue drilling, puncture, and drug delivery. Our work validates the performance of the designed manipulator, laying the foundation for the development of more advanced robotic systems in clinical settings and life science research.

## APPENDIX

$$\mathbf{Rot}(\varphi, \theta, \psi) = \begin{bmatrix} c\psi & -s\psi & 0 \\ s\psi & c\psi & 0 \\ 0 & 0 & 1 \end{bmatrix} \begin{bmatrix} c\theta & 0 & s\theta \\ 0 & 1 & 0 \\ -s\theta & 0 & c\theta \end{bmatrix} \begin{bmatrix} 1 & 0 & 0 \\ 0 & c\varphi & -s\varphi \\ 0 & s\varphi & c\varphi \end{bmatrix} \quad (s1)$$

$$\mathbf{Trans}(x, y, z) = \begin{bmatrix} 1 & 0 & 0 & x \\ 0 & 1 & 0 & y \\ 0 & 0 & 1 & z \\ 0 & 0 & 0 & 1 \end{bmatrix}. \quad (s2)$$

The abbreviations  $c\psi$  represent  $\cos \psi$ ,  $s\psi$  represent  $\sin \psi$ , and the other abbreviations are similar.

## REFERENCES

- [1] G. Z. Yang et al., "The grand challenges of science Robotics," *Sci. Robot.*, vol. 3, no. 14, pp. 1–14, Jan. 2018.
- [2] P. E. Dupont et al., "A decade retrospective of medical robotics research from 2010 to 2020," *Sci. Robot.*, vol. 6, no. 60, pp. 1–15, Nov. 2021.
- [3] T. Haidegger, S. Speidel, D. Stoyanov, and R. M. Satava, "Robot-assisted minimally invasive surgery-surgical robotics in the data age," *Proc. IEEE*, vol. 110, no. 7, pp. 835–846, Jul. 2022.
- [4] H. Saeidi et al., "Autonomous robotic laparoscopic surgery for intestinal anastomosis," *Sci. Robot.*, vol. 7, no. 62, 2022, Art. no. eabj2908.
- [5] S. Weber et al., "Instrument flight to the inner ear," *Sci. Robot.*, vol. 2, no. 4, pp. 1–12, Mar. 2017.
- [6] D. C. Perfetti, S. Kisinde, M. P. Rogers-LaVanne, A. M. Satin, and I. H. Lieberman, "Robotic spine surgery: Past, present, and future," *Spine*, vol. 47, no. 13, pp. 909–921, Jul. 2022.
- [7] T. J. M. van Mulken et al., "first-in-human robotic supermicrosurgery using a dedicated microsurgical robot for treating breast cancer-related lymphedema: A randomized pilot trial," *Nature Commun.*, vol. 11, no. 1, pp. 1–7, Feb. 2020.
- [8] I. I. Iordachita, M. D. De Smet, G. Naus, M. Mitsuishi, and C. N. Riviere, "Robotic assistance for intraocular microsurgery: Challenges and perspectives," *Proc. IEEE*, vol. 110, no. 7, pp. 893–908, Jul. 2022.
- [9] S. Steffens et al., "3D-printed design of a stereotaxic adaptor for the precision targeting of brain structures in infant mice," *Eur. J. Neurosci.*, vol. 55, no. 3, pp. 725–732, Feb. 2022.
- [10] P. R. Olivetti, C. O. Lacefield, and C. Kellendonk, "A device for stereotaxic viral delivery into the brains of neonatal mice," *Biotechniques*, vol. 69, no. 4, pp. 307–312, Oct. 2020.
- [11] G. Q. Shan et al., "Robotic blastocyst biopsy," *IEEE-ASME Trans. Mechatronics*, vol. 28, no. 3, pp. 1372–1383, Jun. 2023.
- [12] T. J. M. van Mulken et al., "Robotic (super) microsurgery: Feasibility of a new master-slave platform in an in vivo animal model and future directions," *J. Surg. Oncol.*, vol. 118, no. 5, pp. 826–831, Oct. 2018.
- [13] T. L. Edwards et al., "First-in-human study of the safety and viability of intraocular robotic surgery," *Nature Biomed. Eng.*, vol. 2, no. 9, pp. 649–656, Sep. 2018.
- [14] M. D. de Smet et al., "Robotic assisted cannulation of occluded retinal veins," *Plos One*, vol. 11, no. 9, Sep. 2016.
- [15] T. L. Hanson, C. A. Diaz-Botia, V. Kharazia, M. M. Maharbiz, and P. N. Sabes, "The 'sewing machine' for minimally invasive neural recording," *bioRxiv*, 2019, Art. no. 578542.
- [16] E. Musk, "An integrated brain-machine interface platform with thousands of channels," *J. Med. Internet Res.*, vol. 21, no. 10, 2019, Art. no. e16194.
- [17] C. Kwan et al., "Co-registration of imaging modalities (MRI, CT and PET) to perform frameless stereotaxic robotic injections in the common marmoset," *Neuroscience*, vol. 480, pp. 143–154, Jan. 2022.
- [18] M. Leveziel, W. Haouas, G. J. Laurent, M. Gauthier, and R. Dahmouche, "MiGriBot: A miniature parallel robot with integrated gripping for high-throughput micromanipulation," *Sci. Robot.*, vol. 7, no. 69, pp. 1–10, Aug. 2022.
- [19] H. McClintock, F. Z. Temel, N. Doshi, J. S. Koh, and R. J. Wood, "The milliDelta: A high-bandwidth, high-precision, millimeter-scale Delta robot," *Sci. Robot.*, vol. 3, no. 14, pp. 1–9, Jan. 2018.
- [20] C. Nwafor, G. J. Laurent, and K. Rabenorosoa, "Miniature parallel continuum robot made of glass: Analysis, design, and proof-of-concept," *IEEE-ASME Trans. Mechatronics*, vol. 28, pp. 2038–2046, Aug. 2023.
- [21] H. Suzuki and R. J. Wood, "Origami-inspired miniature manipulator for teleoperated microsurgery," *Nature Mach. Intell.*, vol. 2, no. 8, pp. 437–446, Aug. 2020.
- [22] T. C. Zhang, Z. Y. Ping, and S. Y. Zuo, "Miniature continuum manipulator with three Degrees-of-Freedom force sensing for retinal microsurgery," *J. Mechanisms Robot.-Trans. ASME*, vol. 13, no. 4, pp. 1–13, Aug. 2021.



- [23] T. Sakai et al., "Design and development of miniature parallel robot for eye surgery," in *Proc. IEEE Eng. Med. Biol. Soc. Conf. Proc.*, 2014, pp. 371–374.
- [24] C. Li, N. K. K. King, and H. Ren, "A skull-mounted robot with a compact and lightweight parallel mechanism for positioning in minimally invasive neurosurgery," *Ann. Biomed. Eng.*, vol. 46, no. 10, pp. 1465–1478, Oct. 2018.
- [25] X. Yang, W. L. Zhu, Z. W. Zhu, and L. M. Zhu, "Design, assessment, and trajectory control of a novel decoupled robotic nanomanipulator," *IEEE-ASME Trans. Mechatron.*, vol. 27, no. 5, pp. 3999–4010, Oct. 2022.
- [26] M. J. Musa, K. Sharma, K. Cleary, and Y. Chen, "Respiratory compensated robot for liver cancer treatment: Design, fabrication, and benchtop characterization," *IEEE-ASME Trans. Mechatron.*, vol. 27, no. 1, pp. 268–279, Feb. 2022.
- [27] Z. F. Huang et al., "Body-mounted MR-conditional robot for minimally invasive liver intervention," *Ann. Biomed. Eng.*, vol. 2024, pp. 1–11, Apr. 2024.
- [28] G. Li et al., "Body-mounted robotic assistant for MRI-guided low back pain injection," *Int. J. Comput. Assist. Radiol. Surg.*, vol. 15, no. 2, pp. 321–331, Feb. 2020.
- [29] G. Deacon et al., "The Pathfinder image-guided surgical robot," *Proc. Inst. Mech. Engineers Part H-J. Eng. Med.*, vol. 224, no. H5, pp. 691–713, 2010.
- [30] G. M. Chen and R. Y. Bai, "Modeling large spatial deflections of slender bisymmetric beams in compliant mechanisms using chained spatial-beam constraint model," *J. Mechanisms Robot.-Trans. ASME*, vol. 8, no. 4, pp. 1–9, Aug. 2016.
- [31] F. L. Ma and G. M. Chen, "Chained beam-constraint-model (CBCM): A powerful tool for modeling large and complicated deflections of flexible beams in compliant mechanisms," 2014.
- [32] D. W. Marquardt, "An algorithm for least-squares estimation of nonlinear parameters," *J. Soc. Ind. Appl. Math.*, vol. 11, no. 2, pp. 431–441, 1963.
- [33] L. Li, J. Wu, H. Ding, and G. Wang, "A 'eye-in-body' integrated surgery robot system for stereotactic surgery," *Int. J. Comput. Assist. Radiol. Surg.*, vol. 14, no. 12, pp. 2123–2135, Jul. 2019.



**Liang Li** received the B.E. degree in mechatronic engineering from Harbin University of Science and Technology, Harbin, China, in 2014, and the M.E. degree in biomedical engineering from the University of Chinese Academy of Sciences, Beijing, China, in 2017, and the Ph.D. degree in biomedical engineering from the Tsinghua University, Beijing, China, in 2021.

He is currently a Lecturer with the School of Biomedical Engineering and Information, Nanjing Medical University, Nanjing, China. His

research interests include surgical robotics and computer-assisted surgery.



**Heng Li** received the B.E. degree in biomedical engineering from Beijing Institute of Technology, Beijing, China, in 2018. He is currently working toward the Ph.D. degree in biomedical engineering with Tsinghua University, Beijing, China.

His research interests are surgical robotics for small animals.



**Chaoye Sui** received the B.E. degree in engineering from the School of Mechanical Engineering, Northeast University, Shenyang, China, in 2021. He is currently working toward the M.E. degree in biomedical engineering with the School of Medicine, Tsinghua University, Beijing, China.

His research interest includes medical surgical robots.



**Hui Ding** received the M.Sc. degree in computer science from the University of science and technology of China, Hefei, China, in 1989.

She is currently a Senior Engineer and the Laboratory Director with the Department of Biomedical Engineering, Tsinghua University, Beijing, China. She is currently a Senior Engineer and the Laboratory Director with the Department of Biomedical Engineering, Tsinghua University, Beijing, China. Her research work includes multimode image guided minimally invasive orthopedic and neurosurgery, ultrasonic fusion imaging.



**Bin Liu** received the B.E. degree in biomedical engineering from Shandong University of Science and Technology, Qingdao, China, in 2006, and the M.E. degree in detection technology and automation equipment from Shandong University of Science and Technology, Qingdao, China, in 2009, and the Ph.D. degree in biomedical engineering from the Southeast University, Nanjing, China, in 2012.

He is currently an Associate Professor with the School of Biomedical Engineering and Information, Nanjing Medical University, Nanjing, China. His research interests are timely detection of critical diseases.



**Jianqing Li** received the B.E. and M.E. degrees in precision instrumentation and the Ph.D. degree in test technology from Southeast University, Nanjing, China, in 1986, 1991, and 2002, respectively.

He is currently a Professor with the School of Biomedical Engineering and Information, Nanjing Medical University, Nanjing, China. His research interests include medical robots and wearable vital sign detection.



**Guangzhi Wang** received the B.E. and M.E. degrees in mechanical engineering and the Ph.D. degree in biomedical engineering from Tsinghua University, Beijing, China, in 1984, 1987, and 2003, respectively.

He is a Tenured Full Professor with the Department of Biomedical Engineering, Tsinghua University, Beijing, China. Since 2015, he has been the Vice President with Chinese Society of Biomedical Engineering. His current research interest includes biomedical image processing,

image based surgical planning and computer aided surgery.